nature communications

Article

https://doi.org/10.1038/s41467-025-61198-y

Manipulating *d*-orbital of Cu single atom site by coordination engineering for selective oxidation of benzene

Received: 8 February 2025

Accepted: 16 June 2025

Published online: 01 July 2025

Check for updates

Shuchun Li[1,5], Changsheng Cao[1,5], Jiabin Chen[2,5], Wen Wen[1], Xuefei Zhang[1], Longji Cui[1], Yuke Li[3], Xing Huang[1,4], Yu Tang[1,2] & Zailai Xie[1,2]

Single-atom catalysts (SACs) enable atomic-level control over active sites, but orbital-level manipulation to steer catalytic behavior remains challenging. Here, we address this issue through *d*-orbital engineering of Cu SACs, achieving simultaneous control over coordination geometry (Cu-N_3) and high metal loading (33.2 wt%) for direct benzene-to-phenol oxidation with H_2O_2. The tri-coordinated Cu SAC (Cu-N_3-33.2) exhibits the highest performance with 85.8% benzene conversion and a turnover frequency of 680.3 h^{-1} at 60 °C, ranking it among the best metal-based catalysts. In-situ ATR-IR spectroscopy and DFT calculations reveal that dynamically formed Cu-O intermediates, driven by *p-d* orbital hybridization between Cu (*d* orbitals) and O (*p* orbitals), lower the H_2O_2 activation barrier by 0.98 eV compared to Cu-N_4 sites. High-density atomic Cu sites prevent over-oxidation by consuming singlet oxygen ($^1O_2$). This work establishes a dual-parameter optimization paradigm, including orbital configuration and site density, redefining design principles for selective oxidation SACs.

The benzene oxidation reaction (BOR) holds a pivotal position in organic synthetic chemistry, given that phenol serves as a crucial raw material and chemical intermediate for numerous industrial applications[1–3]. Currently, the traditional three-step cumene process dominates global phenol production due to its established scalability. However, this process suffers from significant drawbacks, including complex production workflows, low phenol selectivity, high energy demand, and considerable environmental impact[4,5]. Consequently, direct oxidation of benzene to phenol using hydrogen peroxide (H_2O_2) has emerged as a promising yet challenging topic in the pursuit of green and sustainable chemistry, with profound industrial and societal implications[6,7]. The development of innovative and efficient catalysts for BOR is therefore of paramount importance.

Single-atom catalysts (SACs) have garnered substantial attention as an emerging class of materials due to their unique electronic structure and maximum atom utilization, which enable exceptional catalytic performance across a diverse range of reactions[8–13]. Furthermore, the atomic dispersion of active sites in SACs facilitates mechanistic investigations, enabling atomic-level insights into structure-activity relationships[14]. Nevertheless, the inherent variability in the electronic structures of SACs presents challenges in elucidating the reaction mechanism, thereby hindering the systematic study of structure-activity relationships[15–19]. Among the many factors governing the catalytic performance, the *d*-orbital of the metal center plays a decisive role. Adjustments to the coordination structure can alter the electronic state and spatial configuration of the exposed *d*-orbitals, which in turn modulate the adsorption energies, activation barriers, and reaction pathways. Such precise tuning allows for the stabilization of key intermediates and the suppression of undesired side reactions, offering a pathway to enhanced activity and selectivity[20–24].

[1]Key Laboratory of Advanced Carbon-Based Functional Materials (Fujian Province University), Fuzhou University, Fuzhou 350016 Fujian, China. [2]Institute of Molecular Engineering Plus, College of Chemistry, Fuzhou University, Fuzhou 350108, China. [3]Department of Chemistry and Centre for Scientific Modeling and Computation, Chinese University of Hong Kong, Shatin, Hong Kong, China. [4]Electron Microscopy Center, Qingyuan Innovation Laboratory, 362801 Quanzhou, China. [5]These authors contributed equally: Shuchun Li, Changsheng Cao, Jiabin Chen. e-mail: zlxie@fzu.edu.cn

To further optimize SACs, the interplay between metal loading and coordination structure must be systematically explored. Modulating metal loading significantly impacts the intrinsic activity of active sites by altering the local geometry and *d*-orbital of the metal centers through mechanisms such as spin coupling, electron transfer, and charge redistribution[25,26]. SACs with distinct coordination structures can be synthesized through controlled pyrolysis, yet this approach introduces complexities such as the formation of structurally diverse active sites and modifications to the carbon substrate, including defect formation. These challenges complicate the identification of original active sites and the mechanistic understanding of catalytic processes. Consequently, the development of high-loading SACs and the systematic investigation of orbital catalysis are essential for guiding the rational design of more effective catalysts and deepening our understanding of atomic-level catalytic mechanisms[27,28].

Herein, we resolve these challenges through a self-assembly strategy that decouples coordination engineering from metal loading optimization, enabling the systematic exploration of the structure–activity relationship at the orbital level. The optimized Cu-N_3-33.2 catalyst exhibits highly efficient catalytic performance in the selective oxidation of benzene, achieving a high benzene conversion (85.8%) and turnover frequency (680.3 h^{-1}) at 60 °C within 1 h. In addition, the utilization of water as a bi-phase solvent effectively inhibits excessive oxidation of phenol, thereby enhancing selectivity. Mechanistic investigations using quenching experiments and electron paramagnetic resonance (EPR) spectroscopy reveal, that singlet oxygen ($^1O_2$) plays a key role in phenol over-oxidation to *p*-benzoquinone, providing critical insights into the reaction pathway. Furthermore, density functional theory (DFT) calculations and in-situ attenuated total reflection-infrared (ATR-IR) spectroscopy elucidates the mechanism of H_2O_2 activation and benzene oxidation, highlighting the role of the unique *d*-orbital environment of Cu-N_3 in promoting H_2O_2 adsorption and activation. This study offers a simple and efficient strategy for the synthesis of high-loading SACs with well-defined coordination structures, advancing both the understanding of reaction mechanisms and the rational design of selective BOR catalysts.

Results

Structural and morphology characterizations of catalysts

Due to the presence of multiple hydrogen bonds, guanine molecules can act as both hydrogen bond donors and acceptors. This property facilitates the formation of precursors with layered structures through supramolecular self-assembly and π-π interactions (Supplementary Fig. 1)[29]. Moreover, the abundance of N sites in guanine enables the binding of a large number of metal ions, making it possible to prepare SACs with high metal loading. Inspired by this, a series of Cu SACs (Cu-N_x-y, where x represents the coordination number and y denotes the Cu content) were prepared via a two-step process involving the self-assembly of guanine molecules and a subsequent high-temperature carbonization process (Fig. 1a), where the contents of Cu SACs and their coordination numbers can be easily tuned by adjusting the amounts of added Cu^{2+} ions. Meanwhile, the neat N-doped carbon (NC) was also prepared using a similar process without the addition of Cu^{2+} ions. As shown in Supplementary Fig. 2a, b, the powder X-ray

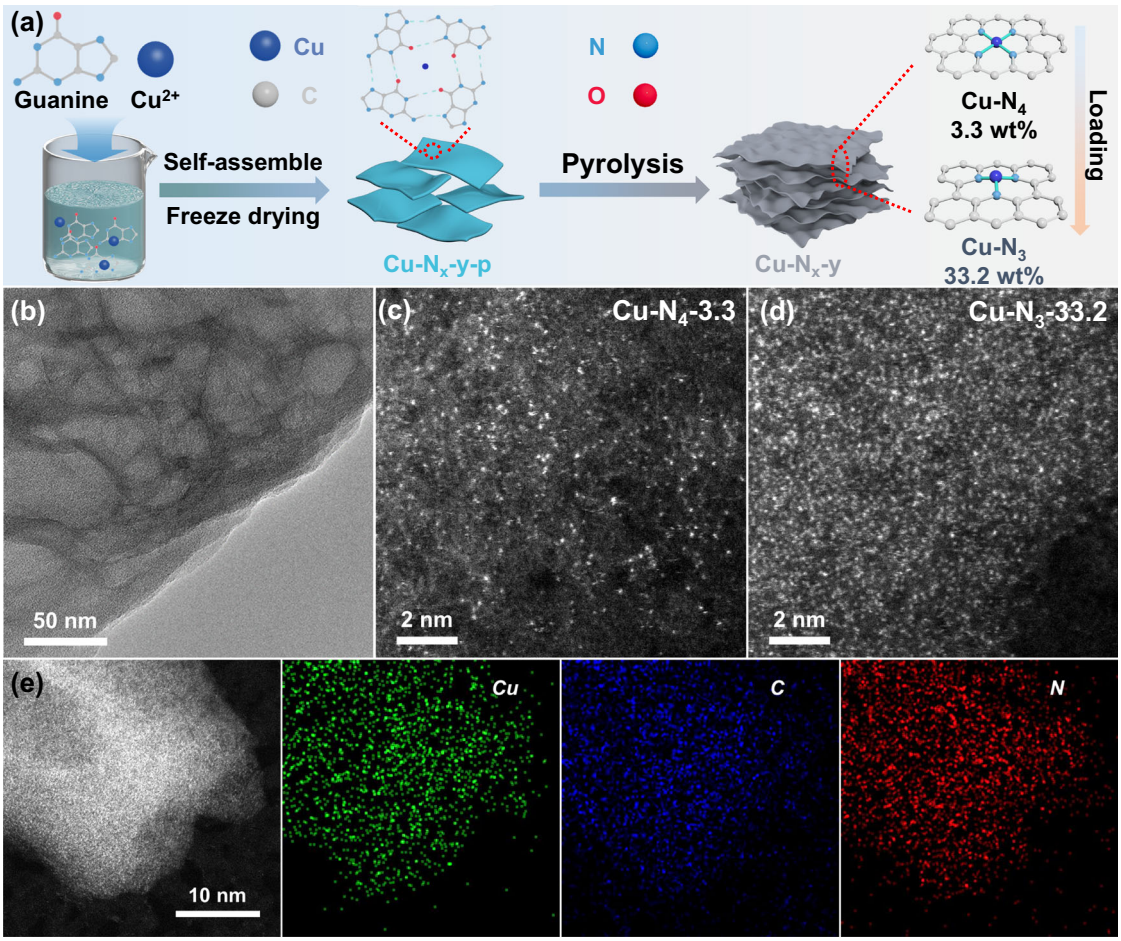

Fig. 1 | Synthesis and characterizations of Cu-N_x-y catalysts. a Schematic illustration for the synthesis of Cu-N_x-y catalysts. **b** TEM image of Cu-N_3-33.2. HAADF-STEM images of (**c**) Cu-N_4-3.3 and (**d**) Cu-N_3-33.2. **e** EDX elemental mapping images of Cu-N_3-33.2. All images in Fig. 1a are original drawings by the authors, created using Autodesk 3ds Max 2025 software. No Autodesk or third-party images were used; permissions not required.

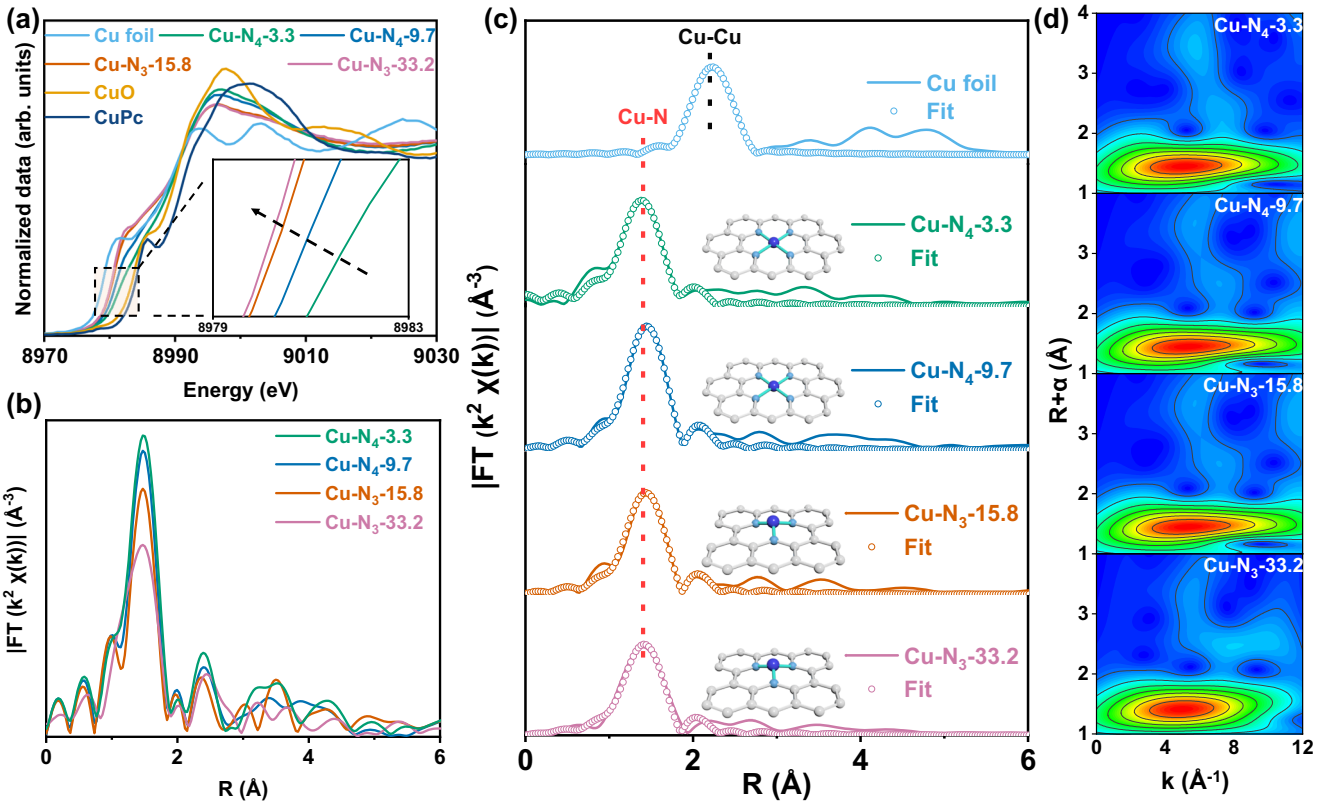

Fig. 2 | Structure characterizations. a Normalized Cu K-edge XANES and (**b**) FT-EXAFS spectra of different Cu-N_x-y catalysts. **c** FT-EXAFS spectra and corresponding fitting EXAFS spectra of Cu foil and different Cu-N_x-y catalysts. **d** Wavelet transform EXAFS plots of different Cu-N_x-y catalysts. All the FT-EXAFS data are presented without phase correction. The grayish-white, light blue and dark blue refer to C, N, and Cu atoms, respectively.

diffraction (PXRD) patterns and Fourier Transform Infrared (FT-IR) spectra of guanine self-assembly precursors (Cu-N_x-y-p) with different Cu^{2+} contents closely resemble those of pristine guanine, indicating that the presence of Cu^{2+} does not affect the structural integrity of guanine. Subsequently, Cu-N_x-y was prepared through a high-temperature pyrolysis process under N_2 environment. Based on inductively coupled plasma optical emission spectrometry (ICP-OES) analysis

(Supplementary Table 1), the Cu content in the as-prepared Cu-N_x-y ranges from 3.3 wt% (Cu-N_4-3.3), 9.7 wt% (Cu-N_4-9.7), 15.8 wt% (Cu-N_3-15.8) to 33.2 wt% (Cu-N_3-33.2), indicating the successful preparation of Cu SACs with controlled metal loading. Notably, only a broad peak centered at $2\theta \approx 26°$ is observed in the PXRD patterns of both NC and all Cu-N_x-y samples, which corresponds to the (002) plane of graphitized carbon (Supplementary Fig. 2c), indicating that Cu might be atomically dispersed over the support. Similarly, during pyrolysis, the active groups of the precursors decompose while retaining certain stable functional groups like C = O and C-N (Supplementary Fig. 2d), which confirms the viability of the in-situ N-doping strategy. Moreover, scanning electron microscopy (SEM, Supplementary Fig. 3) and transmission electron microscopy (TEM, Fig. 1b and Supplementary Fig. 4) images demonstrate that the as-prepared NC and all Cu-N_x-y have a layered nanosheet morphology with

wrinkles and lateral size in microscale. Notably, as shown in Fig. 1c, d and Supplementary Fig. 5, plenty of atomically-scale bright spots, rather than Cu nanoparticles or clusters, were observed in the aberration-corrected high-angle annular dark-field scanning TEM (AC HAADF-STEM) images, which intuitively reflects the atomic dispersion of Cu atoms in Cu-N_4-3.3, Cu-N_4-9.7, Cu-N_3-15.8, and even Cu-N_3-33.2. Meanwhile, energy-dispersive X-ray (EDX) elemental mappings show that C, N, and Cu elements are uniformly distributed throughout the Cu-N_x-y samples (Fig. 1e and Supplementary Fig. 6). Furthermore, Raman spectra of NC and all Cu-N_x-y show the similar D- and G-band intensity ratios (I_D/I_G), suggesting that the introduction of Cu has no effect on the degree of disorder of the samples (Supplementary Fig. 7). Additionally, N_2 adsorption–desorption isotherms (Supplementary Fig. 8) reveal that all Cu-N_x-y samples possess similar BET-specific surface areas, further indicating that the introduction of Cu has no obvious influence on the structure of NC support, which is beneficial for exploring the underlying structure-activity relationship.

The surface chemical compositions and electronic states of NC and Cu-N_x-y were investigated by X-ray photoelectron spectroscopy (XPS). Survey spectra show that C, O and N are present in all samples, while Cu is only present in Cu-N_x-y (Supplementary Fig. 9). In the high-resolution N 1*s* spectra of all samples (Supplementary Fig. 10), the peaks at around 398.5, 399.9, 401.0, and 402.5 eV are ascribed to pyridinic-N, pyrrolic-N, graphitic-N, and N-oxides, respectively[30–32]. Regarding Cu 2*p* spectra (Supplementary Fig. 11), the peaks at around 932.6 and 934.5 eV are attributed to the Cu $2p_{3/2}$ electronic configurations with oxidation states of +2 and +1/0, respectively. This result indicates the oxidation state of Cu atoms in Cu-N_x-y, which is further corroborated by the analysis of the corresponding Cu LMM Auger spectra (Supplementary Fig. 12)[33,34]. Moreover, it is noteworthy that the proportion of Cu^+ species in Cu-N_x-y increases with higher Cu loading, suggesting a gradual reduction in oxidation state. In other words, varying Cu contents in Cu-N_x-y can significantly affect the electronic structure of the atomic Cu centers, which is expected to influence catalytic performance.

To further reveal the local electronic and geometric structures of the Cu centers in Cu-N_x-y, X-ray absorption spectroscopy (XAS) analysis was performed. As shown in the Cu K-edge X-ray absorption near-edge structure (XANES) spectra (Fig. 2a), the absorption energy edges

https://doi.org/10.1038/s41467-025-61198-y

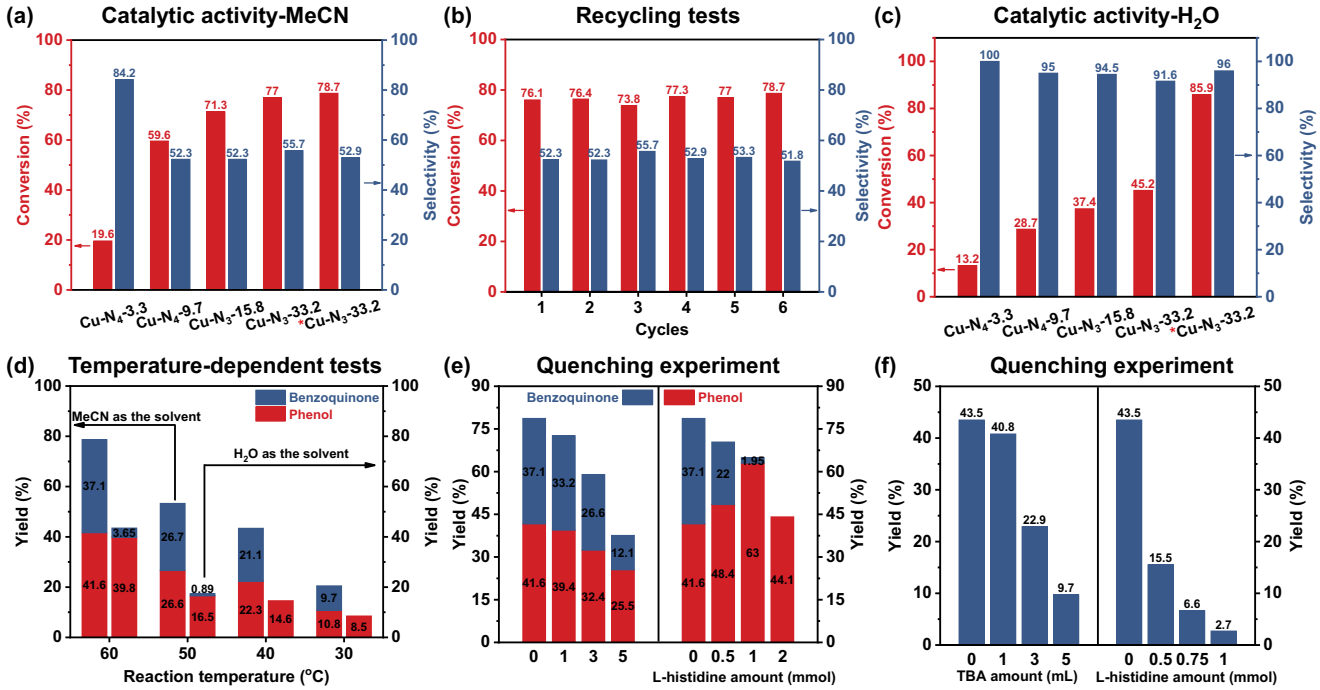

Fig. 3 | BOR performance of the Cu-N_x-y catalysts. a, **c** Catalytic performance of the Cu-N_x-y catalysts for the selective oxidation of benzene to phenol. **b** Recycling performance of Cu-N_3-33.2. **d** Temperature-dependent BOR performance of Cu-N_3-33.2 using different solvents. Catalytic performance of Cu-N_3-33.2 for (**e**) benzene oxidation and (**f**) phenol oxidation in the presence of different quenchers. Reaction conditions: 5 mg catalyst, 0.3 mL benzene, 6 mL solvent (MeCN in (**a**), H_2O in (**c**)), 5 mL H_2O_2, 60 °C, 1 h. *Extend the reaction time to 5 h. MeCN: Acetonitrile. TBA: Tert-butanol.

of all Cu-N_x-y samples fall between those of Cu foil and CuO, implying that the oxidation state of the atomic Cu centers should be between 0 and +2[35,36]. Meanwhile, it can also be observed that the pre-edge absorption energy of Cu-N_x-y shifts towards lower energies with increasing Cu content, suggesting a decrease in the average valence state of Cu centers, which is consistent with the XPS results. Moreover, the *k*2-weighted Fourier-transformed extended X-ray absorption fine structure (FT-EXAFS) spectra show that all Cu-N_x-y samples display one primary peak at ~1.47 Å, which is attributed to the Cu-N scattering in the first coordination shell (Fig. 2b and Supplementary Fig. 13a). As compared to CuO and Cu foil, the absence of Cu-O-Cu (2.5 Å) and Cu-Cu (2.2 Å) coordination confirms the atomic dispersion of Cu atoms in all Cu-N_x-y samples.

Therefore, it can be concluded that Cu centers in all Cu-N_x-y samples are coordinated with N atoms. Quantitative fitting of the EXAFS spectra (Fig. 2c and Supplementary Table 2) shows that the Cu centers in Cu-N_4-3.3 and Cu-N_4-9.7 are tetra-coordinated with Cu-N_4 configuration, while those in Cu-N_3-15.8 and Cu-N_3-33.2 are tri-coordinated with Cu-N_3 configuration, revealing that changing the metal loading in Cu SACs leads to different coordination structures of the Cu centers, thereby affecting the valence state and electronic structure of the Cu atoms. Furthermore, the wavelet transform (WT) EXAFS contour plot of Cu foil shows an intensity maximum at about 7.8 $Å^{-1}$ (Supplementary Fig. 13b), which is attributed to the Cu-Cu coordination. In contrast, all Cu-N_x-y samples only present an intensity maximum at around 4.8 $Å^{-1}$ (Fig. 2d and Supplementary Fig. 13c, d), which can be attributed to the Cu-N path, further endorsing the atomic dispersion of Cu atoms.

Benzene oxidation performances of catalysts

The benzene oxidation reaction (BOR) using H_2O_2 as the oxidant was conducted at 60 °C with Cu-N_x-y catalysts. Before evaluating the catalytic performance of these catalysts in BOR, several control experiments were performed, and the results were displayed in Supplementary Table 3. The conversion of benzene hardly occurred in the absence of H_2O_2, indicating that H_2O_2 is essential for the selective oxidation of benzene to phenol. Moreover, the conversion of benzene was almost 0 in the absence of Cu SACs or when using NC as the catalyst, demonstrating that the Cu sites are the authentic active sites for BOR. Therefore, it can be concluded that BOR is a Cu-catalyzed process, with H_2O_2 as an essential reactant. Considering the high Cu loadings (up to 33.2 wt%) of the as-prepared Cu-N_x-y, these catalysts are expected to provide a substantial number of active sites for the efficient oxidation of benzene to phenol. Figure 3a displays the catalytic activity of various Cu SACs at 60 °C for 1 h using acetonitrile (MeCN) as the solvent. As expected, the benzene conversion gradually increased from 19.6% to 78.7% with the increase of Cu loading from 3.3 to 33.2 wt%. To explore the relationship between BOR performance and H_2O_2 concentration, the BOR performance of Cu-N_3-33.2 was evaluated using different amount of H_2O_2. The results show that increasing the H_2O_2 concentration will increase the benzene conversion but will also slightly sacrifice the selectivity (Supplementary Fig. 14a). Moreover, the utilization of H_2O_2 of different catalysts was calculated under the same reaction conditions (i.e., adding 5 mL H_2O_2). The results show that Cu-N_3-33.2 with best catalytic activity also exhibits the highest H_2O_2 utilization, reaching 32.6% (Supplementary Fig. 14b), indicating that catalysts with higher BOR activity have higher H_2O_2 activation efficiency. To further reveal whether the improvement in catalytic performance is solely due to the increase in Cu loading, we kept the Cu content in the catalysts consistent and further evaluated their BOR performance. Surprisingly, as shown in Supplementary Table 4, the Cu SACs with Cu-N_3 centers exhibited much higher activity compared to those with Cu-N_4 centers. Correspondingly, the calculated turnover frequency (TOF) and mass activity of the Cu-N_x-y catalysts also increased with higher Cu loading. Particularly, Cu-N_3-33.2, with a Cu loading of 33.2 wt%, exhibited impressive TOF and mass activity values of 680.3 h^{-1} and 1927.6 mmol·g^{-1}·h^{-1}, respectively, distinguishing it among previously reported Cu SACs for the selective

oxidation of benzene with H_2O_2 (Supplementary Fig. 15 and Supplementary Table 5)[1,16,37–45]. Meanwhile, under the same coordination structure, Cu-N_x-y catalysts with higher Cu loading also showed higher activity, indicating that the exceptional catalytic activity of Cu-N_3-33.2 is attributed to its unique low-coordination structure and higher number of active sites. Besides its highly efficient catalytic activity, Cu-N_3-33.2 also exhibited remarkable stability under the test conditions. As shown in Fig. 3b, both benzene conversion and phenol selectivity have no significant changes after six cycles. More importantly, TEM image, PXRD patterns, as well as normalized Cu K-edge XANES and FT-EXAFS spectra reveal that after the reaction, the Cu atoms in Cu-N_3-33.2 remain atomically dispersed without aggregation, and both the morphology and coordination structure are preserved compared to their original states (Supplementary Fig. 16), exclude the formation of CuO_x cluster after reaction. In addition, ICP-OES analysis result shows that the Cu content (29.5 wt%) in Cu-N_3-33.2 after the stability test is comparable to that before the reaction, further demonstrating its satisfactory stability.

Although the Cu-N_x-y catalysts exhibit excellent catalytic activity and stability in BOR, their selectivity for phenol is poor and decrease significantly with the increase of Cu loading (Fig. 3a). Specifically, the phenol selectivity of Cu-N_3-33.2 is only 52.9%. Since MeCN and H_2O_2 are miscible, the catalyst and oxidant in the reaction system are in full contact with benzene, thereby efficiently converting it to phenol. However, the instability of phenol and its high solubility in MeCN make it easy to be further oxidized to *p*-benzoquinone. Therefore, timely separation of the generated phenol is expected to significantly improve its selectivity. Considering the poor solubility of benzene in water, BOR will proceed at the benzene-water interface when water is used as the solvent[46]. Although this may affect catalytic activity, this unique interfacial reaction is advantageous for product separation, thereby improving phenol selectivity. As predicted, the benzene conversion of all Cu-N_x-y catalysts decreased significantly when using water as the solvent. In contrast, the phenol selectivity of all Cu-N_x-y catalysts dramatically increased (Fig. 3c). Especially for Cu-N_3-33.2, the phenol selectivity increased from 52.9% to 91.6%. More notably, when the reaction time was extended to 5 h, the conversion of benzene reached 85.9%, which is comparable to the activity observed when MeCN was used as the solvent. Meanwhile, the phenol selectivity remains as high as 96%, which is significantly better than the latter, revealing that the interfacial effect is conducive to the separation of products, thereby improving the selectivity of products. Since the generated phenol is slightly soluble in water, a small amount of *p*-benzoquinone byproduct can also be detected when water is used as the solvent. To gain a deeper understanding of the relationship between the interfacial effect and phenol selectivity, temperature-dependent catalytic activity tests were conducted. As shown in Fig. 3d, the activity of Cu-N_3-33.2 in both MeCN and water solvents gradually decreased as the reaction temperature decreased. It is noteworthy that the phenol selectivity hardly changes with temperature when MeCN is used as the solvent. In contrast, when water is used as the solvent, the phenol selectivity gradually increase with decreasing reaction temperature, and impressively, the phenol selectivity can reach 100% at 40 °C, which is attributed to the decrease in the solubility of phenol in water as the temperature decreases. Notably, as shown in Supplementary Fig. 17a, both benzene conversion and phenol selectivity of Cu-N_3-33.2 have no significant changes after five cycles using H_2O as solvent. Moreover, the PXRD pattern and HRTEM image after stability testing showed that no Cu-based metal clusters or nanoparticles were formed in Cu-N_3-33.2 (Supplementary Fig. 17b, c), demonstrating its excellent structural and activity stability in water. This study highlights the selective oxidation of benzene to phenol in a thermocatalytic system using water as solvent, offering cost-effective and environmentally sustainable pathways for advancing industrial phenol synthesis.

BOR mechanism study

Previous studies have shown that Cu SACs are able to activate H_2O_2 and generate reactive oxygen species (ROSs) including ·OH and $O_2^{\cdot-}$ radicals, thus initiating the efficient oxidation of benzene to phenol[12,41,47]. Unfortunately, the resulting phenol is also susceptible to further oxidation by these ROSs. To further reveal the underlying reaction mechanism, quenching experiments and electron paramagnetic resonance (EPR) spectra were employed to detect the ROSs during the reaction. As a kind of quencher for ·OH radicals, the addition of tert-butanol (TBA) influences the benzene conversion but has no significant effect on phenol selectivity (Fig. 3e), suggesting that ·OH radicals are absent in the reaction system or is hardly responsible for the over-oxidation of phenol. Furthermore, it is well known that EPR spectroscopy are usually employed to detect the ·OH and $O_2^{\cdot-}$ radicals using 5, 5-dimethyl-1-pyrroline-noxide (DMPO) as the scavenger[48]. However, as shown in Supplementary Fig. 18a, no obvious signals belonging to DMPO-OH· or DMPO-$O_2^{\cdot-}$ species are observed, which means that almost no ·OH and $O_2^{\cdot-}$ radicals are generated in the reaction system. Moreover, L-histidine is usually used to trap holes singlet oxygen ($^1O_2$) species. It is noteworthy that although the addition of L-histidine reduces the conversion of benzene, it significantly improves the phenol selectivity. Impressively, after adding 2 mmol of L-histidine into the reaction system, the phenol selectivity can even reach 100%, indicating that $^1O_2$ species are primarily responsible for the over-oxidation of phenol to *p*-benzoquinone. Furthermore, EPR spectroscopy solidly confirms the presence of $^1O_2$ species in the reaction system (Supplementary Fig. 18b). To further reveal the roles of $^1O_2$ species in the BOR process, the catalytic performance of Cu-N_3-33.2 toward phenol oxidation reaction was evaluated under similar reaction conditions. As displayed in Fig. 3f, the phenol conversion is 43.5% in the absence of L-histidine. However, with the addition of L-histidine, the phenol conversion dropped sharply, further confirming that the $^1O_2$ species is the authentic ROS caused further oxidation of phenol.

To elucidate the reaction mechanism of the selective oxidation of benzene to phenol over Cu single-atom catalysts (SACs), a detailed pathway is proposed based on experimental observations and previous reports[41,47]. As illustrated in Fig. 4a, the reaction starts with the adsorption and activation of H_2O_2 on the Cu-N_x active sites to form O-Cu-N_x intermediates (step I). Subsequently, the C_6H_6 molecules adsorbed on the Cu-O sites (step II) and forms the Cu-N_x-C_6H_5OH intermediates via a hydrogen transfer process (step III). Finally, the catalytic cycle is completed after the desorption of C_6H_5OH molecules and the regeneration of the Cu-N_x sites (step IV). Besides, to gain a deeper understanding of the effect of coordination structures of Cu SACs on the catalytic performance, the catalytic activities of all Cu-N_x-y samples were evaluated by adjusting the catalyst amount to maintain a consistent Cu content. As clearly shown in Supplementary Fig. 19, the samples with Cu-N_3 coordination configuration exhibit much higher activity compared to those with Cu-N_4 coordination configuration under identical reaction conditions. According to the XPS and XANES results, both Cu^{2+} and Cu^+ species exist in all Cu-N_x-y samples, and the proportion of Cu^+ species increases with the increase of Cu loading. Further in-depth XPS analysis showed that the Cu^+/Cu^{2+} ratio was positively correlated with the BOR activity (Supplementary Fig. 20). Moreover, we therefore investigated the genuine active species indirectly by studying the BOR activity of Cu SACs with pure Cu (II)-N_4 structure. Results show that 2.4-Cu_1/NOC (a previous reported Cu SACs with pure Cu (II)-N_4 structure)[12] and commercial copper phthalocyanine (CuPc, with pure Cu (II)-N_4 structure) cannot effectively activate benzene under the same reaction conditions of the Cu-N_x-y catalysts (Supplementary Table 6), confirming that low-coordinated Cu (I)-N_3 structures should be the genuine active species in our reaction system despite the minor presence of Cu (II)-N_4 species. To further reveal the effect of the coordination configuration of atomic Cu

https://doi.org/10.1038/s41467-025-61198-y

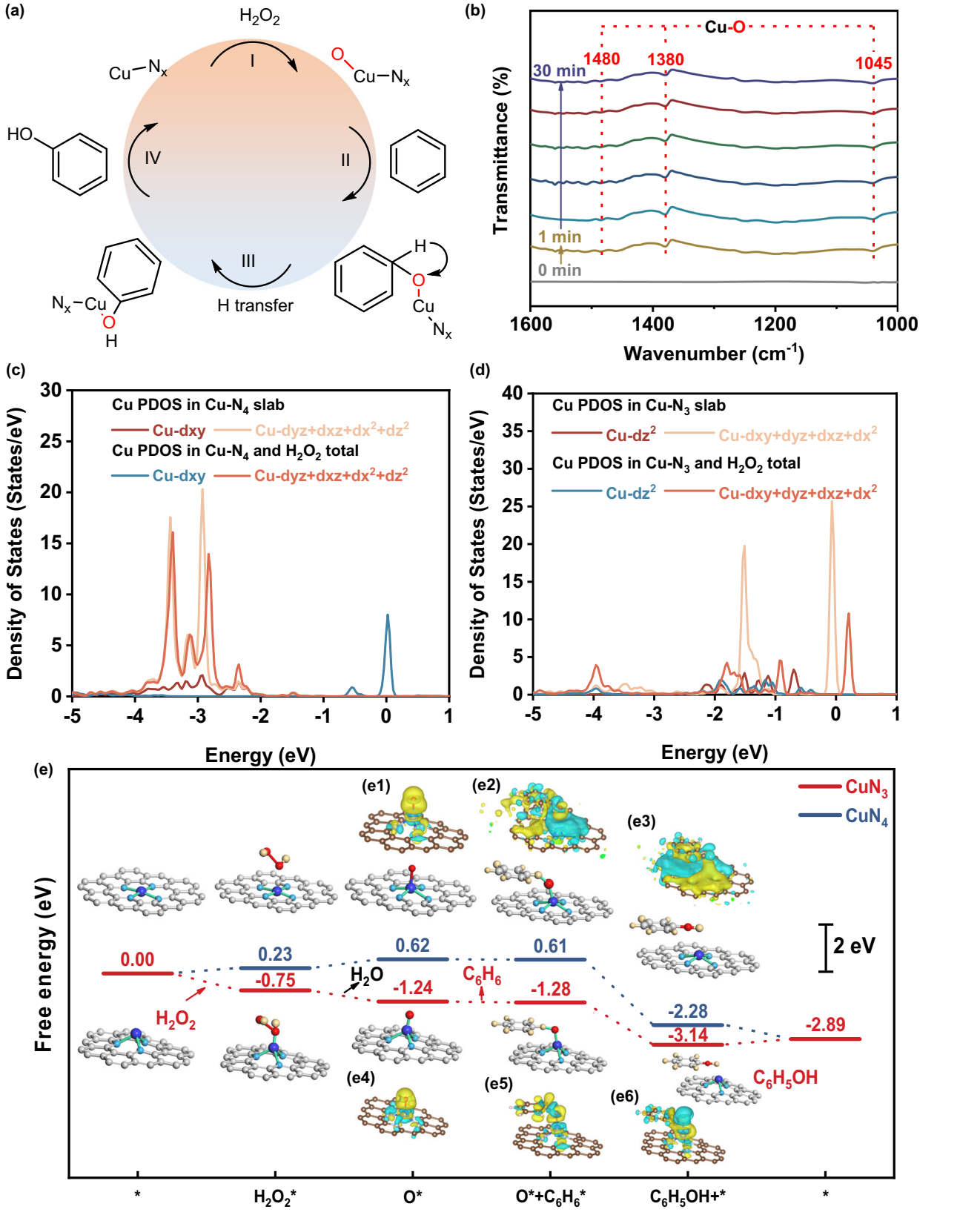

Fig. 4 | Catalytic reaction mechanism analysis. a The proposed BOR mechanisms over the Cu-N_x-y catalyst. **b** In-situ *IR* spectra of Cu-N_3-33.2. **c**, **d** Projected density of states (pDOS) of the Cu centers on the CuN_3 and CuN_4 interfaces before and after H_2O_2 adsorption. **e** Free energy diagrams of benzene oxidation to phenol on Cu-N_3 and Cu-N_4 sites. **e1**-**e6** The charge density difference of Cu-N_3, Cu-N_4 in BOR. Yellow and cyan isosurfaces indicate the electron accumulation and depletion, respectively.

centers on the catalytic performance, in-situ *IR* spectroscopy analysis was first performed. As shown in Fig. 4b and Supplementary Fig. 21, characteristic peaks corresponding to Cu-O species (1045, 1380 and 1480 cm^{-1}) were detected during the reaction, indicating the formation of Cu-O species in presence of H_2O_2[49–51]. According to previous reports, the in-situ formed Cu-O species should be the authentic active species for selective oxidation of selective oxidation of benzene to phenol[41,47]. It is noteworthy that the in-situ *IR* signals of Cu-O species from Cu-N_3-33.2 are stronger than those of Cu-N_4-3.3, indicating that the Cu-N_3 coordination configuration is prone to produce more Cu-O active species, which is beneficial to promote the reaction. In addition, control experiments showed that CuO or metallic Cu loaded on NC support (CuO/NC and Cu NPs/NC) exhibit much inferior BOR performance compared to Cu-N_3-33.2 (Supplementary Fig. 22 and Table 6), confirming that the in-situ generated O-Cu-N_x species should be the real active site for the efficient conversion of benzene to phenol.

To further corroborate these experimental findings and elucidate the underlying mechanisms, density functional theory (DFT) calculations were performed. Analysis of the electronic structure of Cu atoms in the Cu-N_4 and Cu-N_3 centers (Fig. 4c, d and Supplementary Fig. 23), suggests that the electronic interactions between the O atom in H_2O_2 and Cu atom in these two centers are different. Specifically, For the CuN_4 configuration, the relaxed structure reveals a Cu atom embedded within four N atoms, exhibiting D_4h symmetry and strong crystal field effects. Notably, the four coordinated N atoms interact with the d_{xy} orbitals of the Cu atom in a "head-to-head" manner, resulting in *d*-orbital energy splitting, where the d_{xy} orbitals is located at a higher energy level than the remaining four orbitals. Moreover, the calculation results further show that the d_{xy} orbitals located at the Fermi level determine the physicochemical properties of the Cu site. However, despite the energy level alignment, the steric mismatch between the d_{xy} orbitals of the Cu atom and the *p* orbitals O atoms prevents effective bonding, while other *d* orbitals suitable for bonding are located at significantly deeper energy levels. Therefore, as shown in Fig. 4c, the energy levels and density of states (DOS) of the d_{xy} orbitals of Cu atom show almost no changes even after H_2O_2 adsorption, indicating weak electron exchange due to orbital incompatibility. In contrast, for the CuN_3 coordination configuration, the theoretically optimized structure shows that the Cu atom is embedded in a trigonal planar configuration (C_{3v} symmetry) formed by three N atoms, with an average Cu−N bond length of 1.90 Å, which is highly consistent with the experimental EXAFS results (1.89–1.91 Å, Supplementary Table 2) (deviation < 0.01 Å), verifying the reliability of the calculation model. Compared with the planar D_4h symmetry of CuN_4, the reduction in the N coordination number in CuN_3 causes the Cu atom to protrude slightly from the carbon substrate plane, forming a more open coordination environment. This geometric distortion not only shortens the distance between Cu and adsorbates (such as H_2O_2), but also promotes the more efficient hybridization of the *d* orbitals of Cu atom and the *p* orbitals of O atom. As shown in Fig. 4d, part of the *d* orbitals of Cu atom in the Cu-N_3 coordination configuration are pushed above the Fermi level after H_2O_2 adsorption, which indicates that these *d* orbitals match the *p* orbitals of O atom in H_2O_2, resulting in a strong electronic interaction. Through the pDOS analysis, it was found that the *p* orbitals of the O atom in the H_2O_2 molecule and the *d* orbitals of the Cu atom (especially the *dz*2 orbitals) show obvious overlap in energy distribution, indicating that there is a strong electronic coupling between O atom and the Cu atom. Furthermore, through the two-dimensional (2D) charge density difference analysis (Supplementary Fig. 24), it can be intuitively observed that H_2O_2 molecule gains electrons from the Cu atom during the adsorption process, which directly confirms the orbital matching mechanism and the redistribution of interface charges. Meanwhile, it seems like the Cu dz^2 orbitals signatures shifted below the Fermi energy upon the adsorption of the H_2O_2 molecule. We believe that this phenomenon may originate from the strong hybridization between the *p* orbital of the O atom in the H_2O_2 molecule and the dz^2 orbital of Cu, which causes the energy of some electronic states to shift downward. This interaction not only changes the *d* orbitals distribution of Cu atoms but also reflects the dynamic adjustment of the electronic structure during the adsorption process. Ultimately, the strong electronic interaction between the *d* orbitals of Cu atom in the Cu-N_3 coordination configuration and the *p* orbitals of O atom in H_2O_2 endow it with stronger adsorption of H_2O_2 compared with that in the Cu-N_4 coordination configuration, which is confirmed with the much lower adsorption energy of H_2O_2 on the CuN_3-slab (Supplementary Fig. 25). The mechanism of the difference in adsorption strength was further revealed by calculating the d-band center of the Cu atom. The results show that the *d*-band centers of the Cu-N_3 and Cu-N_4 coordination structures are located at −1.5673 and −2.7682 eV, respectively. Since the *d*-band center of Cu-N_3 is closer to the Fermi level, it exhibits a significantly enhanced H_2O_2 adsorption ability, which is highly consistent with experimental observations and theoretical predictions. This finding clearly reveals the crucial role of the coordination structure on the electronic structure and catalytic activity of Cu atoms in Cu-N-C catalysts. The adsorption energy of H_2O_2 on CuN_3 (−117.87 kJ/mol) is significantly lower than on CuN_4 (-24.27 kJ/mol) (Supplementary Fig. 25), directly linked to the electronic structure differences. The higher *d*-band center of CuN_3 (−1.5673 eV vs. −2.77 eV for CuN_4) enhances H_2O_2 adsorption by strengthening the *p-d* hybridization between O (*p* orbitals) and Cu (*d* orbitals), as evidenced by the overlapping pDOS (Fig. 4d and Supplementary Fig. 23). This electronic synergy lowers the H_2O_2 activation efficiency, rationalizing the superior activity of CuN_3. Furthermore, the Bader charge analysis and calculated adsorption energies of these systems were further performed. For the interaction with C_6H_6O molecules, the charge transfer amounts is 0.09 e^- in Cu-N_3, while that in Cu-N_4 is 0.04 e^-. For the case of H_2O_2, Cu-N_3 exhibits a charge transfer of 1.86 e^-, which is significantly higher than the 0.17 e^- observed in Cu-N_4. These quantitative results confirm that the Cu-N_3 configuration has superior charge transfer activity compared to the Cu-N_4 configuration, which is consistent with its higher adsorption energy for H_2O_2, indicating an optimized electronic interaction with the reactants. This difference may originate from the lower coordination number of the Cu-N_3 configuration, where the unsaturated coordination structure enhances the tunability of the reactants to the electronic structure of Cu atoms, thereby improving the catalytic activity.

Moreover, As shown in Supplementary Table 7, Bader charge analysis reveals that the oxidation states of Cu in CuN_3, CuN_4 and CuO are +0.52 (11 − 10.4775 = 0.5225), +0.82 (11 − 10.1828 = 0.8172) and +1.00 (11 − 9.996 = 1.004), respectively. Bader charge analysis, while not equivalent to formal oxidation states, reveals the relative electron density distribution around Cu centers, corroborating the XANES-derived oxidation state trends. Moreover, the projected density of states (pDOS) analysis shows that the *d* orbitals of Cu atom in CuO display broader and flatter features, which is attributed to the significantly enhanced ligand field strength at high oxidation states, thereby strengthening the hybridization between *d* orbitals of Cu atom and ligands (e.g., O atoms). In contrast, the sharper pDOS peak of Cu in CuN_3 suggest stronger electron localization, which may be due to its lower oxidation state and weaker ligand field effects, thereby retaining *d* electrons closer to the Cu atoms(Supplementary Fig. 26). Combined with the catalytic performance, the localized electronic structure in CuN_3 can promote the generation of O-Cu-N_3 active intermediates, thus improving the BOR performance. Kinetic isotope experiment revealed that the conversion of deuterated benzene was comparable to that of untreated benzene, indicating that the activation of C-H bonds in BOR is not the rate-determining step (Supplementary Fig. 27). Notably, the free-energy diagram of the pathways for the generation of phenol shows that the adsorption of H_2O_2 is crucial for the oxidation of benzene to phenol, and Cu SACs with Cu-N_3 coordination

configuration are more conducive to promoting the reaction (Fig. 4e). Furthermore, the electron density difference maps show that the Cu-N_3 coordination configuration is more responsive to electron transfer than the Cu-N_4 coordination configuration (Fig. 4e1-e6 and Supplementary Fig. 28), indicating that the Cu SACs with Cu-N_3 coordination configuration has a stronger and more favorable interaction with the reactants. Consequently, the open coordination environment and unique electron density distribution of the Cu-N_3 coordination configuration enable it to promote electron transfer and enhance the interaction with reactants, resulting in better catalytic performance. We further investigated the H_2O_2 activation pathways, including the generation of $^1O_2$ species. As shown in Supplementary Fig. 29, the energy barrier for the formation of $^1O_2$ on the Cu-N_3 site is very high, implying that the in-situ generated O-Cu-N_3 should preferentially react with benzene to form phenol, while excess H_2O_2 may promote the generation of $^1O_2$, leading to formation of over-oxidation products (e.g., benzoquinone), which is consistent with the experimental results shown in Supplementary Fig. 14a. Although Cu-N_4 exhibits a high tendency to form $^1O_2$, its actual generation is restricted by the inherently high energy barrier for the formation of O-Cu-N_4 formation from Cu-N_4, thereby limiting the generation of $^1O_2$ in Cu-N_x-y catalysts with Cu-N_4 structure. The combination of in-situ IR spectroscopy and DFT calculations provides compelling evidence that the Cu-N_3 coordination configuration in Cu SACs is more effective for the selective oxidation of benzene to phenol, due to its ability to generate more active Cu-O species and facilitate stronger electronic interactions with reactants.

Discussion

In summary, we have successfully designed and synthesized tri- and tetra-coordinated Cu SACs with ultra-high metal loadings via a simple two-step process involving supramolecular self-assembly and high-temperature carbonization. The results show that the electronic states at the orbital level can be manipulated to optimize catalytic performance by controlling metal loading within carbon-based supports. The optimized tri-coordinated Cu SAC with ultra-high metal loading of up to 33.2 wt% exhibited a superior catalytic performance for the selective oxidation of benzene to phenol. We have revealed that the in-situ generated Cu-O species are revealed to be the active centers for the oxidation of benzene to phenol, while the in-situ generated $^1O_2$ species are a decisive factor in the undesirable over-oxidation of phenol to *p*-benzoquinone. This work provides deep insights into the precise tuning of catalytic reactivity of SACs by electron orbital engineering.

Methods

Synthesis of Cu-N_x-y

Guanine (5 g) and $Cu(NO_3)_2{\cdot}3H_2O$ (0.21/0.67/0.95/1.63 g) were uniformly dispersed in 50 mL of deionized water and heated at 100 °C for 12 h in an oil bath. The resulting suspension was rapidly frozen using liquid nitrogen and subsequently freeze-dried to yield the precursor. The precursor was then subjected to pyrolysis at 700 °C for 2 h under protection of N_2, with a heating rate of 1 °C min^{-1}, producing Cu single-atom catalysts, designated as Cu-N_4-3.3, Cu-N_4-9.7, Cu-N_3-15.8, and Cu-N_3-33.2. Neat nitrogen-doped carbon material (NC) was synthesized using the same procedure without the addition of $Cu(NO_3)_2{\cdot}3H_2O$.

Catalytic test

For a typical liquid phase benzene oxidation reaction, 5 mg catalyst, 0.3 mL benzene, 5 mL H_2O_2 and 6 mL solvent were mixed in a 48 mL thick-walled pressure flask and reacted at 60 °C at a stirring speed of 500 rpm for 1 h. Reactant and product concentrations were analyzed by gas chromatography-mass spectrometer (GC-MS) using tetradecane as the internal standard.

$$\text{Benzene conversion}\,(\%) = 100\% - \frac{\text{moles of unreacted phenol}}{\text{moles of initial benzene}} \times 100\%$$

$$\text{Phenol selectivity}\,(\%) = \frac{\text{moles of formed phenol}}{\text{total moles of formed phenol and byproducts}} \times 100\%$$

$$\text{Yield}\,(\%) = \frac{\text{moles of formed phenol}}{\text{total moles of formed phenol and byproducts}} \times 100\%$$

$$\text{TOF} = \frac{\Delta n_{benzene}}{t \times n_{Cu}}$$

Where $\Delta n_{benzene}$ is converted benzene (mol); t is the reaction time (h); n_{Cu} is the amount of Cu-based active sites (mol).

X-ray absorption spectra analysis

The obtained XAS spectra was processed in Athena (version 0.9.26) for background, pre-edge line and post-edge line calibrations. Then Fourier transformed fitting was carried out in Artemis (version 0.9.26). The k^2 weighting, k-range of 3–14 $Å^{-1}$ and R range of 1 ~ 3 Å were used for the fitting of Cu foil; k-range of 2–10 $Å^{-1}$ and R range of 1 ~ 2 Å were used for the fitting of samples. The four parameters, coordination number, bond length, Debye-Waller factor and E_0 shift (CN, R, ΔE_0) were fitted without anyone was fixed, the σ^2 was set. For Wavelet Transform analysis, the χ(k) exported from Athena was imported into the Hama Fortran code. The parameters were listed as follow: R range, 1–4 Å, k range, 0–15 $Å^{-1}$ for samples; k weight, 2; and Morlet function with $\kappa = 10$, $\sigma = 1$ was used as the mother wavelet to provide the overall distribution.

Density functional theory calculation details

First-principle Density functional theory (DFT) calculations with the spin-polarized consideration were carried out within the density functional theory framework. The projector-augmented wave (PAW)[52] method and the generalized gradient approximation (GGA) for the exchange correlation energy functional, as implemented in the Vienna ab initio simulation package (VASP 5.4.4)[53,54] were used. The GGA calculation was performed with the Perdew–Burke–Ernzerhof (PBE) exchange-correlation potential[55]. A plane-wave cutoff energy of 400 eV was used. Grimmes's DFT-D3 dispersion correction was used to describe the van der waals interaction[56]. A 6 × 6 graphene supercell with 15 Å vacuum layer was first constructed. A 3 × 3 K-points was used in all these calculations. Dipole correction was taken into consideration in the slab calculation[57].

The adsorption free energy (ΔG_{ads}) is obtained by:

$$\Delta G_{ads} = \Delta E + \Delta E_{ZPE} - T\Delta S$$

Where ΔE is the energy difference of the reactants and products, obtained from DFT calculations; ΔE_{ZPE} and ΔS are the contributions to the free energy from the zero-point vibration energy and entropy, respectively. T is the temperature (298 K). The free energy for gas phase water is calculated at 0.035 bars. The free energy for other molecules is calculated at 1 bar.

Data availability

The source data are provided in the Source data file. The data supporting this study are available for the corresponding author upon request. Source data are provided with this paper.

References

1. Pan, Y. et al. Regulating the coordination structure of single-atom Fe-N_xC_y catalytic sites for benzene oxidation. *Nat. Commun.* **10**, 4290 (2019).
2. Chen, X., Zhang, J., Fu, X., Antonietti, M. & Wang, X. Fe-g-C_3N_4-Catalyzed oxidation of benzene to phenol using hydrogen peroxide and visible light. *J. Am. Chem. Soc.* **131**, 11658–11659 (2009).

3. Niwa, S.-i et al. A one-step conversion of benzene to phenol with a palladium membrane. *Science* **295**, 105–107 (2002).
4. Morimoto, Y., Bunno, S., Fujieda, N., Sugimoto, H. & Itoh, S. Direct hydroxylation of benzene to phenol using hydrogen peroxide catalyzed by nickel complexes supported by pyridylalkylamine ligands. *J. Am. Chem. Soc.* **137**, 5867–5870 (2015).
5. Tanev, P. T., Chibwe, M. & Pinnavaia, T. J. Titanium-containing mesoporous molecular sieves for catalytic oxidation of aromatic compounds. *Nature* **368**, 321–323 (1994).
6. Yang, J.-H. et al. Direct catalytic oxidation of benzene to phenol over metal-free graphene-based catalyst. *Energy Environ. Sci.* **6**, 793–798 (2013).
7. Zhang, H. et al. Enhancing chemical reactions in a confined hydrophobic environment: an NMR study of benzene hydroxylation in carbon nanotubes. *Chem. Sci.* **4**, 1075–1078 (2013).
8. Qiao, B. et al. Single-atom catalysis of CO oxidation using Pt_1/FeO_x. *Nat. Chem.* **3**, 634–641 (2011).
9. Kaiser, S. K., Chen, Z., Faust Akl, D., Mitchell, S. & Pérez-Ramírez, J. Single-atom catalysts across the periodic table. *Chem. Rev.* **120**, 11703–11809 (2020).
10. Liu, H. et al. Reconstructing the coordination environment of Fe/Co dual-atom sites towards efficient oxygen electrocatalysis for Zn–air batteries. *Angew. Chem. Int. Ed.* **64**, e202419595 (2024).
11. Zhang, H. et al. Tailoring oxygen reduction reaction kinetics of Fe–N–C catalyst via spin manipulation for efficient zinc–air batteries. *Adv. Mater.* **36**, 2400523 (2024).
12. Jin, H. et al. Understanding the density-dependent activity of Cu single-atom catalyst in the benzene hydroxylation reaction. *ACS Catal.* **13**, 1316–1325 (2023).
13. Hai, X. et al. Geminal-atom catalysis for cross-coupling. *Nature* **622**, 754–760 (2023).
14. Yin, P. et al. Single cobalt atoms with precise N-coordination as superior oxygen reduction reaction catalysts. *Angew. Chem. Int. Ed.* **55**, 10800–10805 (2016).
15. Wang, X. et al. Regulation of coordination number over single Co sites: triggering the efficient electroreduction of CO_2. *Angew. Chem. Int. Ed.* **57**, 1944–1948 (2018).
16. Zhu, Y. et al. A cocoon silk chemistry strategy to ultrathin N-doped carbon nanosheet with metal single-site catalysts. *Nat. Commun.* **9**, 3861 (2018).
17. Wan, J. et al. IIn situ phosphatizing of triphenylphosphine encapsulated within metal–organic frameworks to design atomic $Co_1–P_1N_3$ interfacial structure for promoting catalytic performance. *J. Am. Chem. Soc.* **142**, 8431–8439 (2020).
18. Zhang, J. et al. Tuning the coordination environment in single-atom catalysts to achieve highly efficient oxygen reduction reactions. *J. Am. Chem. Soc.* **141**, 20118–20126 (2019).
19. Rong, X., Wang, H.-J., Lu, X.-L., Si, R. & Lu, T.-B. Controlled synthesis of a vacancy-defect single-atom catalyst for boosting CO_2 electroreduction. *Angew. Chem. Int. Ed.* **59**, 1961–1965 (2020).
20. Guo, H. & Guo, S. Strain engineering of multimetallic nanomaterials for advanced electrocatalysis. *CCS Chem.* **7**, 326–344 (2025).
21. Qi, C. et al. Modulating electronic structures of iron clusters through orbital rehybridization by adjacent single copper sites for efficient oxygen reduction. *Angew. Chem. Int. Ed.* **62**, e202308344 (2023).
22. Li, X., Chen, T., Yang, B. & Xiang, Z. Fundamental understanding of electronic structure in FeN_4 site on electrocatalytic activity via dz-orbital-driven charge tuning for acidic oxygen reduction. *Angew. Chem. Int. Ed.* **62**, e202215441 (2023).
23. Ramaswamy, N., Tylus, U., Jia, Q. & Mukerjee, S. Activity descriptor identification for oxygen reduction on nonprecious electrocatalysts: linking surface science to coordination chemistry. *J. Am. Chem. Soc.* **135**, 15443–15449 (2013).
24. Yuan, K. et al. Boosting oxygen reduction of single iron active sites via geometric and electronic engineering: nitrogen and phosphorus dual coordination. *J. Am. Chem. Soc.* **142**, 2404–2412 (2020).
25. Shan, J. et al. Metal-metal interactions in correlated single-atom catalysts. *Sci. Adv.* **8**, eabo0762 (2022).
26. Jin, Z. et al. Understanding the inter-site distance effect in single-atom catalysts for oxygen electroreduction. *Nat. Catal.* **4**, 615–622 (2021).
27. Chang, J. et al. Synthesis of ultrahigh-metal-density single-atom catalysts via metal sulfide-mediated atomic trapping. *Nat. Synth.* **3**, 1427–1438 (2024).
28. Wang, Y. et al. General negative pressure annealing approach for creating ultra-high-loading single atom catalyst libraries. *Nat. Commun.* **15**, 5675 (2024).
29. Otero, R. et al. Guanine quartet networks stabilized by cooperative hydrogen bonds. *Angew. Chem. Int. Ed.* **44**, 2270–2275 (2005).
30. Ran, J. et al. Endowing g-C_3N_4 membranes with superior permeability and stability by using acid spacers. *Angew. Chem. Int. Ed.* **58**, 16463–16468 (2019).
31. Wang, D. et al. Coordination-engineered Cu–N_x single-site catalyst for enhancing oxygen reduction reaction. *ACS Appl. Energy Mater.* **2**, 6497–6504 (2019).
32. Zhang, H. et al. Single atomic iron catalysts for oxygen reduction in acidic media: particle size control and thermal activation. *J. Am. Chem. Soc.* **139**, 14143–14149 (2017).
33. Cao, J. et al. Strongly coupled 2D transition metal chalcogenide-MXene-carbonaceous nanoribbon heterostructures with ultrafast ion transport for boosting sodium/potassium ions storage. *Nano-Micro Lett.* **13**, 113 (2021).
34. Wagh, N. K. et al. Densely colonized isolated Cu-N single sites for efficient bifunctional electrocatalysts and rechargeable advanced Zn-air batteries. *Appl Catal. B. Environ.* **268**, 118746 (2020).
35. Bao, H. et al. Isolated copper single sites for high-performance electroreduction of carbon monoxide to multicarbon products. *Nat. Commun.* **12**, 238 (2021).
36. Wang, X. et al. Uncoordinated amine groups of metal–organic frameworks to anchor single Ru sites as chemoselective catalysts toward the hydrogenation of quinoline. *J. Am. Chem. Soc.* **139**, 9419–9422 (2017).
37. Shen, Q. et al. Ionic-liquid-assisted synthesis of metal single-atom catalysts for benzene oxidation to phenol. *Sci. China Mater.* **65**, 163–169 (2022).
38. Deng, D. et al. A single iron site confined in a graphene matrix for the catalytic oxidation of benzene at room temperature. *Sci. Adv.* **1**, e1500462 (2015).
39. Chen, W. et al. Dynamic evolution of nitrogen and oxygen dual-coordinated single atomic copper catalyst during partial oxidation of benzene to phenol. *Nano Res.* **15**, 3017–3025 (2022).
40. Liu, J. et al. Direct observation of metal oxide nanoparticles being transformed into metal single atoms with oxygen-coordinated structure and high-loadings. *Angew. Chem. Int Ed.* **60**, 15248–15253 (2021).
41. Che, W. et al. Out-of-plane single-copper-site catalysts for room-temperature benzene oxidation. *Angew. Chem. Int Ed.* **63**, e202403017 (2024).
42. Liu, Y. et al. Atomically dispersed Cu anchored on nitrogen and boron codoped carbon nanosheets for enhancing catalytic performance. *ACS Appl Mater. Interfaces* **13**, 61047–61054 (2021).
43. Zhang, T. et al. Preassembly strategy to fabricate porous hollow carbonitride spheres inlaid with single Cu–N_3 sites for selective oxidation of benzene to phenol. *J. Am. Chem. Soc.* **140**, 16936–16940 (2018).
44. Zhou, H. et al. Cation-exchange induced precise regulation of single copper site triggers room-temperature oxidation of benzene. *J. Am. Chem. Soc.* **142**, 12643–12650 (2020).

45. Zhang, M. et al. Metal (Hydr)oxides@polymer core–shell strategy to metal single-atom materials. *J. Am. Chem. Soc.* **139**, 10976–10979 (2017).
46. Xie, J. et al. Highly selective oxidation of benzene to phenol with air at room temperature promoted by water. *Nat. Commun.* **14**, 4431 (2023).
47. Zhang, T. et al. Regulating electron configuration of single Cu sites via unsaturated N,O-coordination for selective oxidation of benzene. *Nat. Commun.* **13**, 6996 (2022).
48. Li, S., Ke, Y., Zhang, X., Wu, S. & Xie, Z. Iron carbide nanoparticles encapsulated in guanine-derived carbon for peroxymonosulfate activation. *Sep Purif. Technol.* **338**, 126570 (2024).
49. Dong, S. & Spiro, T. G. Ground- and excited-state mapping of plastocyanin from resonance raman spectra of isotope-labeled proteins. *J. Am. Chem. Soc.* **120**, 10434–10440 (1998).
50. Liu, C. et al. In situ reconstruction of Cu–N coordinated MOFs to generate dispersive Cu/Cu_2O nanoclusters for selective electroreduction of CO_2 to C_2H_4. *ACS Catal.* **12**, 15230–15240 (2022).
51. Tao, W. et al. Reductive NO coupling at dicopper center via a $[Cu_2(NO)_2]^{2+}$ diamond-core intermediate. *J. Am. Chem. Soc.* **144**, 22633–22640 (2022).
52. Blochl, P. E. Projector augmented-wave method. *Phys. Rev. B* **50**, 17953–17979 (1994).
53. Kresse, G. & Hafner, J. Ab initio molecular dynamics for open-shell transition metals. *Phys. Rev. B* **48**, 13115–13118 (1993).
54. Kresse, G. & Furthmüller, J. Efficiency of ab-initio total energy calculations for metals and semiconductors using a plane-wave basis set. *Comput Mater. Sci.* **6**, 15–50 (1996).
55. Perdew, J. P., Burke, K. & Ernzerhof, M. Generalized gradient approximation made simple. *Phys. Rev. Lett.* **77**, 3865–3868 (1996).
56. Grimme, S., Antony, J., Ehrlich, S. & Krieg, H. A consistent and accurate ab initio parametrization of density functional dispersion correction (DFT-D) for the 94 elements H-Pu. *J. Chem. Phys.* **132**, 154104 (2010).
57. Neugebauer, J. & Scheffler, M. Adsorbate-substrate and adsorbate-adsorbate interactions of Na and K adlayers on Al (111). *Phys. Rev. B* **46**, 16067–16080 (1992).

Acknowledgements

This work was financed by the National Natural Science Foundation of China (22372039) and the Natural Science Foundation of Fujian Province (2021J06010).

Author contributions

S.L. conceived and performed the experiments, collected and analyzed data and wrote the paper. J.C. and Y.L. conceived and performed the DFT calculations and wrote the DFT section. W.W., L.C. and X.Z. joined the discussion of data and gave useful suggestions. C.C., X.H., Y.T. and Z.X. conceived the idea, supervised the project work and led the data analysis and discussion and prepared and finalized the paper. All the authors commented on the manuscript and have given approval to the final version of the manuscript.

Competing interests

The authors declare no competing interests.

Additional information

Supplementary information The online version contains supplementary material available at https://doi.org/10.1038/s41467-025-61198-y.

Correspondence and requests for materials should be addressed to Zailai Xie.

Peer review information *Nature Communications* thanks Aiqin Wang and the other, anonymous, reviewer(s) for their contribution to the peer review of this work. A peer review file is available.